Draft version June 5, 2019
Typeset using LaTeX **preprint** style in AASTeX62

Constraining M_ν with the Bispectrum I: Breaking Parameter Degeneracies

ChangHoon Hahn,[1,2,*] Francisco Villaescusa-Navarro,[3] Emanuele Castorina,[2,1] and Roman Scoccimarro[4]

[1] *Lawrence Berkeley National Laboratory, 1 Cyclotron Rd, Berkeley CA 94720, USA*
[2] *Berkeley Center for Cosmological Physics, University of California, Berkeley, CA 94720, USA*
[3] *Center for Computational Astrophysics, Flatiron Institute, 162 5th Avenue, New York, NY 10010, USA*
[4] *Center for Cosmology and Particle Physics, Department of Physics, New York University, NY 10003, New York, USA*

(Dated: `DRAFT --- 87c9896 --- 2019-06-05 --- NOT READY FOR DISTRIBUTION`)

ABSTRACT

Massive neutrinos suppress the growth of structure below their free-streaming scale and leave an imprint on large-scale structure. Measuring this imprint allows us to constrain the sum of neutrino masses, M_ν, a key ingredient for particle physics beyond the Standard Model. However, degeneracies with cosmological parameters limit the constraining power of standard two-point clustering statistics. In this work, we investigate whether we can break these parameter degerancies and constrain M_ν with the next higher-order correlation function, the bispectrum. We first examine the degeneracy between M_ν and σ_8 using 800 N-body simulations from the HADES suite and demonstrate that the redshift-space halo bispectrum helps break this degeneracy. Next, we quantify the information content of the redshift-space halo bispectrum in a Fisher matrix forecast that includes M_ν and cosmological parameters Ω_m, Ω_b, h, n_s, and σ_8. This is the first N-body simulation based Fisher matrix forecast of cosmological parameters using the bispectrum. More importantly, for $k_\mathrm{max} = 0.2$ and 0.5 we find

Keywords: cosmology: —

1. INTRODUCTION

CH: very brief into on neutrinos Brief intro on the impact of massive active neutrinos on the matter powerspectrum and how that's detectable with CMB and LSS

Quick summary of current cosmology constraints and where they come from.

Talk about the CMB-LSS lever arm. The degeneracy between As and tau and how that's a bottleneck short thing about how τ is hard to constrain. Fortunately the imprint of neutrinos on the matter distribution leaves imprints on clustering. So with clustering measurements alone we can derive constraints on M_ν and at the very least tighten constraints.

* hahn.changhoon@gmail.com

Brief summary of previous works that look at the powerspectrum. Then Discuss the shortcomings of the powerspectrum only analysis– Not good enough.

However, we don't have to settle for just two point statistics, three-point statistics such as the bispectrum and 3PCF...

In Section blah

CH: List plans for paper 2

2. HADES AND QUIJOTE SIMULATION SUITES

We use a subset of the HADES[1] and Quijote simulation suites. Below, we briefly describe these simulations; a brief summary of the simulations can be found in Table 1. The HADES simulations start from Zel'dovich approximated initial conditions generated at $z = 99$ using the Zennaro et al. (2017) rescaling method and follow the gravitational evolution of $N_{\rm cdm} = 512^3$ CDM, plus $N_\nu = 512^3$ neutrino particles (for massive neutrino models), to $z = 0$. They are run using the GADGET-III TreePM+SPH code (Springel 2005) in a periodic $(1h^{-1}{\rm Gpc})^3$ box. All of the HADES simulations share the following cosmological parameter values, which are in good agreement with Planck constraints Ade et al. (2016): $\Omega_{\rm m}$=0.3175, $\Omega_{\rm b}$=0.049, Ω_Λ=0.6825, n_s=0.9624, h=0.6711, and $k_{\rm pivot} = 0.05\ h{\rm Mpc}^{-1}$.

The HADES suite includes models with degenerate massive neutrinos of different masses: $M_\nu =$ 0.06, 0.10, and 0.15 eV. These massive neutrino models are run using the "particle method", where neutrinos are described as a collisionless and pressureless fluid and therefore modeled as particles, same as CDM (Brandbyge et al. 2008; Viel et al. 2010). HADES also includes models with massless neutrino and different values of σ_8 to examine the $M_\nu - \sigma_8$ degeneracy. The σ_8 values were chosen to match either σ_8^m or σ_8^c — σ_8 computed with respect to total matter (CDM + baryons + ν) or CDM + baryons — of the massive neutrino models: $\sigma_8 = 0.822, 0.818, 0.807$, and 0.798. Each model has 100 independent realizations and we focus on the snapshots saved at $z = 0$. Halos closely trace the CDM+baryon field rather than the total matter field and neutrinos have negligible contribution to halo masses (*e.g.* Ichiki & Takada 2012; Castorina et al. 2014; LoVerde 2014; Villaescusa-Navarro et al. 2014). Hence, dark matter halos are identified in each realization using the Friends-of-Friends algorithm (FoF; Davis et al. 1985) with linking length $b = 0.2$ on the CDM + baryon distribution; only halos with masses $> 3.2 \times 10^{13} h^{-1} M_\odot$ are included. For further details on the HADES simulations, we refer readers to Villaescusa-Navarro et al. (2018).

In addition to HADES, we use simulations from the Quijote simulation suite, a set of 23,000 N-body simulations that in total contain more than 3.3 trillion (3.3×10^{12}) particles over a volume of $23000(h^{-1}{\rm Gpc})^3$. These simulations were constructed to quantify the information content of different cosmological observables using Fisher matrix forecasting (*e.g.* Section 4.2). They are therefore designed to accurately calculate the covariance matrices of observables and the derivatives of observables with respect to cosmological parameters. The suite considers 6 cosmological parameters: $\Omega_{\rm m}$, $\Omega_{\rm b}$, h, n_s, σ_8, and M_ν.

[1] https://franciscovillaescusa.github.io/hades.html

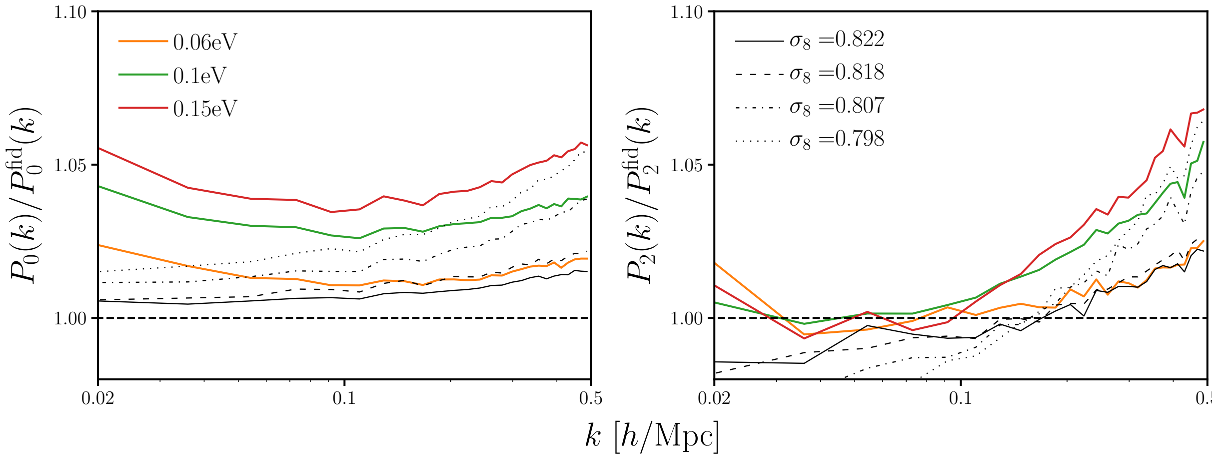

Figure 1. Impact of M_ν and σ_8 on the redshift-space halo power spectrum monopole and quadrupole measured using the HADES simulation suite. M_ν and σ_8 produce almost identical effects on halo clustering on small scales ($k > 0.1\,h/\mathrm{Mpc}$). This degeneracy can be partially broken through the quadrupole; however, *M_ν and σ_8 produce almost the same effect on two-point clustering — within a few percent.*

To calculate covariance matrices, Quijote includes $N_{\rm cov} = 15,000$ N-body simulations run at a fiducial cosmology ($\Omega_{\rm m}$=0.3175, $\Omega_{\rm b}$=0.049, h=0.6711, n_s=0.9624, σ_8=0.834, and M_ν=0.0 eV). It also includes sets of 500 N-body simulations run at different cosmologies where only one parameter is varied from the fiducial cosmology at a time for the derivatives. Along $\Omega_{\rm m}$, $\Omega_{\rm b}$, h, n_s, and σ_8, the fiducial cosmology is adjusted by either a small step above and below the fiducial value. Along M_ν, because the derivative of certain observable with respect to M_ν is noisy, Quijote includes sets of 500 simulations for $M_\nu = 0.1$, 0.2, and 0.4 eV. In Table 1, we list the cosmologies included in the Quijote suite.

The intial conditions for all Quijote simulations were generated at $z = 127$ using 2LPT for simulations with massless neutrinos and the Zel'dovich approximation for massive neutrinos. Like HADES, the initial conditions of simulations with massive neutrinos take their scale-dependent growth factors/rates into account using the Zennaro et al. (2017) method. From the initial conditions, all of the simulations follow the gravitational evolution of 512^3 dark matter particles, and 512^3 neutrino particles (for massive neutrino models), to $z = 0$ using Gadget-III TreePM+SPH code (same as HADES). The simulations run at the fiducial cosmology for covariance matrix estimation are standard N-body simulations. However, the rest are paired fixed simulations, which greatly reduce cosmic variance without introducing bias for a large set of statistics (Angulo & Pontzen 2016; Pontzen et al. 2016; Villaescusa-Navarro et al. 2018). We confirm that the paired fixed simulations do not introduce any bias for the redshift-space halo bispectrum (the observable we consider in this paper). For further details on the Quijote simulations, we refer readers to Villaescusa-Navarro et al. (in preparation).

3. BISPECTRUM

We're interested in breaking parameter degeneracies that limit the constraining power on M_ν of two-point clustering analyses using three-point clustering statistics — *i.e.* the bispectrum. In

Table 1. Specifications of the HADES and Quijote simulation suites.

Name	M_ν (eV)	Ω_m	Ω_b	h	n_s	σ_8^m ($10^{10}h^{-1}M_\odot$)	σ_8^c ($10^{10}h^{-1}M_\odot$)	realizations
				HADES suite				
Fiducial	0.0	0.3175	0.049	0.6711	0.9624	0.833	0.833	100
	0.06	0.3175	0.049	0.6711	0.9624	0.819	0.822	100
	0.10	0.3175	0.049	0.6711	0.9624	0.809	0.815	100
	0.15	0.3175	0.049	0.6711	0.9624	0.798	0.806	100
	0.0	0.3175	0.049	0.6711	0.9624	0.822	0.822	100
	0.0	0.3175	0.049	0.6711	0.9624	0.818	0.818	100
	0.0	0.3175	0.049	0.6711	0.9624	0.807	0.807	100
	0.0	0.3175	0.049	0.6711	0.9624	0.798	0.798	100
				Qujiote suite				
Fiducial	0.0	0.3175	0.049	0.6711	0.9624	0.834	0.834	15,000
M_ν^+	$\underline{0.1}$	0.3175	0.049	0.6711	0.9624	0.834	0.834	500
M_ν^{++}	$\underline{0.2}$	0.3175	0.049	0.6711	0.9624	0.834	0.834	500
M_ν^{+++}	$\underline{0.4}$	0.3175	0.049	0.6711	0.9624	0.834	0.834	500
Ω_m^+	0.0	$\underline{0.3275}$	0.049	0.6711	0.9624	0.834	0.834	500
Ω_m^-	0.0	$\underline{0.3075}$	0.049	0.6711	0.9624	0.834	0.834	500
Ω_b^+	0.0	0.3175	$\underline{0.051}$	0.6711	0.9624	0.834	0.834	500
Ω_b^-	0.0	0.3175	$\underline{0.047}$	0.6711	0.9624	0.834	0.834	500
h^+	0.0	0.3175	0.049	$\underline{0.6911}$	0.9624	0.834	0.834	500
h^-	0.0	0.3175	0.049	$\underline{0.6511}$	0.9624	0.834	0.834	500
n_s^+	0.0	0.3175	0.049	0.6711	$\underline{0.9824}$	0.834	0.834	500
n_s^-	0.0	0.3175	0.049	0.6711	$\underline{0.9424}$	0.834	0.834	500
σ_8^+	0.0	0.3175	0.049	0.6711	0.9624	$\underline{0.849}$	$\underline{0.849}$	500
σ_8^-	0.0	0.3175	0.049	0.6711	0.9624	$\underline{0.819}$	$\underline{0.819}$	500

Top: The HADES suite includes sets of 100 N-body simulations with degenerate massive neutrinos of $M_\nu =$ 0.06, 0.10, and 0.15 eV as well as sets of simulations with massless neutrino and $\sigma_8 = 0.822$, 0.818, 0.807, and 0.798 to examine the $M_\nu - \sigma_8$ degeneracy. **Bottom**: The Quijote suite includes 15,000 N-body simulations at the fiducial cosmology to accurately estimate the covariance matrices. It also includes sets of 500 paired fixed simulations at different cosmologies, where only one parameter is varied from the fiducial value (underlined), to estimate derivatives of observables along the cosmological parameters.

this section, we describe the bispectrum estimator used throughout the paper. We focus on the bispectrum monopole ($\ell = 0$) and use an estimator that exploits Fast Fourier Transpforms (FFTs). Our estimator is similar to the estimators described in Scoccimarro (2015); Sefusatti et al. (2016); we also follow their formalism in our description below. Although Sefusatti et al. (2016) and Scoccimarro

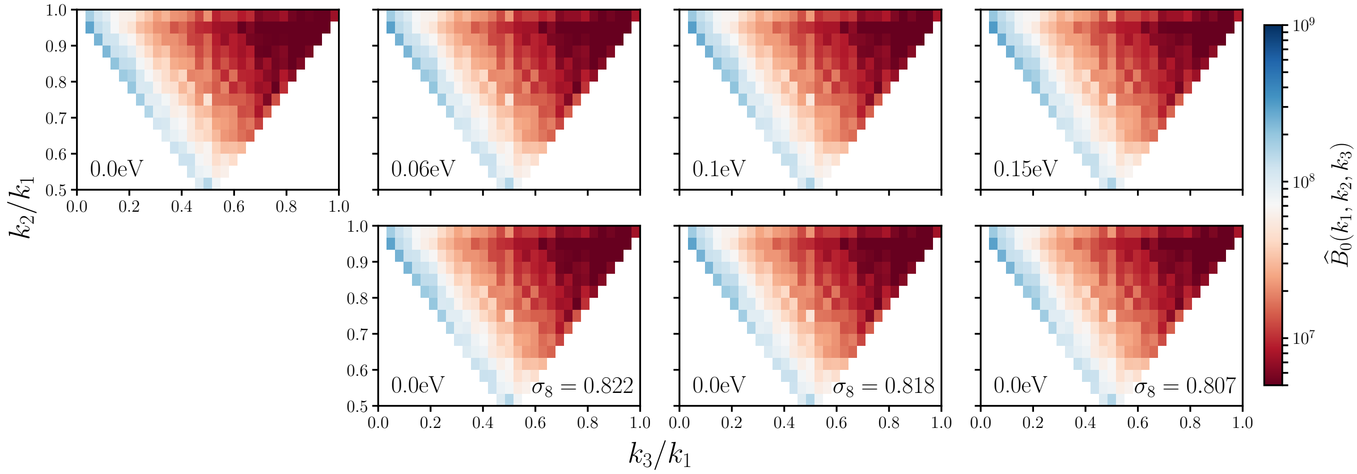

Figure 2. The redshift-space halo bispectrum, $\widehat{B}_0(k_1, k_2, k_3)$, as a function of triangle configuration shape for $M_\nu = 0.0, 0.06, 0.10$, and $0.15\,\text{eV}$ (upper panels) and $\sigma_8 = 0.822, 0.818$, and 0.807 (lower panels). The HADES simulations of the top and bottom panels in the three right-most columns, have matching σ_8 values (Section 2). We describe the triangle configuration shape by the ratio of the triangle sides: k_3/k_1 and k_2/k_1. The upper left bin contains squeezed triangles ($k_1 = k_2 \gg k_3$); the upper right bin contains equilateral triangles ($k_1 = k_2 = k_3$); and the bottom center bin contains folded triangles ($k_1 = 2k_2 = 2k_3$). We include all triangle configurations with $k_1, k_2, k_3 \le k_{\rm max} = 0.5\ h/\text{Mpc}$. and use the $\widehat{B}_0$ estimator in Section 3.

(2015) respectively describe estimators in redshift- and real-space, since we focus on the bispectrum monopole, we note that there is no difference.

To measure the bispectrum of our halo catalogs, we begin by interpolating the halo positions to a grid, $\delta(\boldsymbol{x})$ and Fourier transforming the grid to get $\delta(\boldsymbol{k})$. We use a fourth-order interpolation to interlaced grids, which has advantageous anti-aliasing properties (Hockney & Eastwood 1981; Sefusatti et al. 2016) that allow unbias measurements up to the Nyquist frequency. Then using $\delta(\boldsymbol{k})$, we measure the bispectrum monopole as

$$\widehat{B}_{\ell=0}(k_1, k_2, k_3) = \frac{1}{V_B} \int_{k_1} {\rm d}^3 q_1 \int_{k_2} {\rm d}^3 q_2 \int_{k_3} {\rm d}^3 q_3\ \delta_{\rm D}(\boldsymbol{q}_{123})\ \delta(\boldsymbol{q}_1)\ \delta(\boldsymbol{q}_2)\ \delta(\boldsymbol{q}_3) - B^{\rm SN}_{\ell=0} \tag{1}$$

$\delta_{\rm D}$ above is a Dirac delta function and hence $\delta_{\rm D}(\boldsymbol{q}_{123}) = \delta_{\rm D}(\boldsymbol{q}_1 + \boldsymbol{q}_2 + \boldsymbol{q}_3)$ ensures that the $\boldsymbol{q}_i$ triplet actually form a closed triangle. Each of the integrals above represent an integral over a spherical shell in k-space with radius δk centered at $\boldsymbol{k}_i$ — *i.e.*

$$\int_{k_i} {\rm d}^3 q \equiv \int_{k_i - \delta k/2}^{k_i + \delta k/2} {\rm d}q\ q^2 \int {\rm d}\Omega. \tag{2}$$

V_B is a normalization factor proportional to the number of triplets $\boldsymbol{q}_1$, $\boldsymbol{q}_2$, and $\boldsymbol{q}_3$ that can be found in the triangle bin defined by k_1, k_2, and k_3 with width δk:

$$V_B = \int_{k_1} {\rm d}^3 q_1 \int_{k_2} {\rm d}^3 q_2 \int_{k_3} {\rm d}^3 q_3\ \delta_{\rm D}(\boldsymbol{q}_{123}) \tag{3}$$

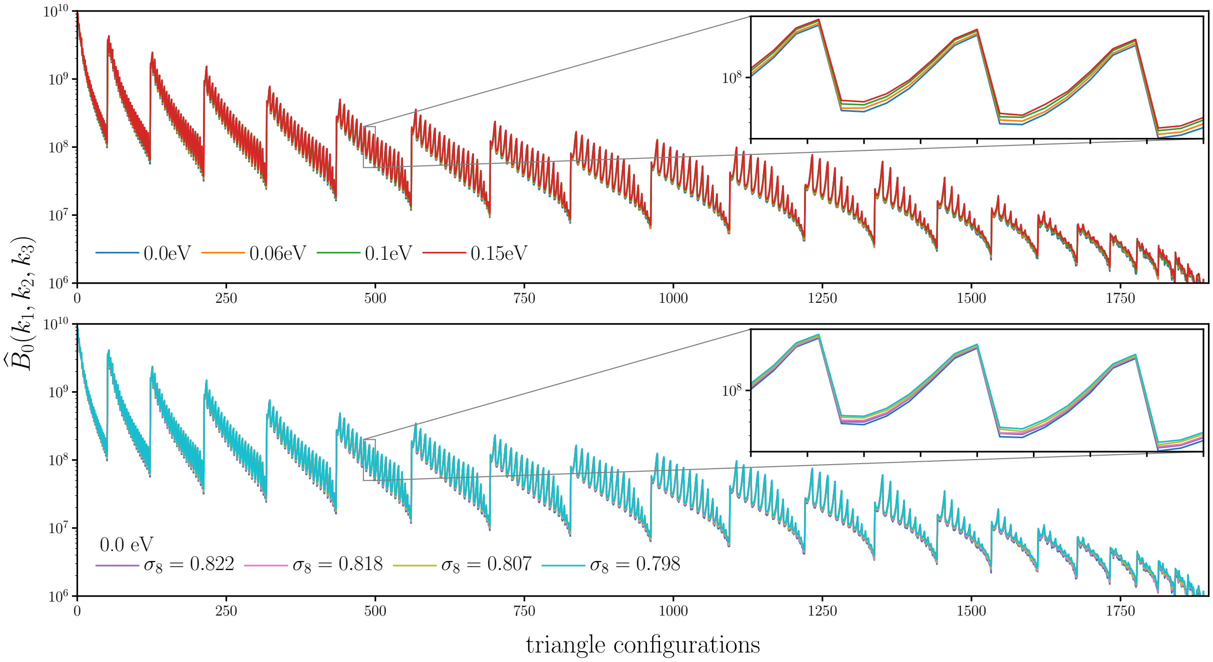

Figure 3. The redshift-space halo bispectrum, $\widehat{B}_0(k_1, k_2, k_3)$, as a function of triangle configurations for $M_\nu = 0.0, 0.06, 0.10,$ and $0.15\,\mathrm{eV}$ (top panel) and $M_\nu = 0.0$ eV, $\sigma_8 = 0.822, 0.818, 0.807,$ and 0.798 (lower panel). We include all possible triangle configurations with $k_1, k_2, k_3 \leq k_{\max} = 0.5\ h/\mathrm{Mpc}$ where we order the configurations by looping through k_3 in the inner most loop and k_1 in the outer most loop satisfying $k_1 \leq k_2 \leq k_3$. In the insets of the panels we zoom into triangle configurations with $k_1 = 0.113$, $0.226 \leq k_2 \leq 0.283$, and $0.283 \leq k_3 \leq 0.377\ h/\mathrm{Mpc}$.

Lastly, $B^{\mathrm{SN}}_{\ell=0}$ is the correction for the Poisson shot noise, which contributes due to the self-correlation of individual objects:

$$B^{\mathrm{SN}}_{\ell=0}(k_1, k_2, k_3) = \frac{1}{\bar{n}}\big(P_0(k_1) + P_0(k_2) + P_0(k_3)\big) + \frac{1}{\bar{n}^2}. \tag{4}$$

$\bar{n}$ is the number density of objects (halos) and P_0 is the powerspectrum monopole.

In order to evaluate the integrals in Eq. 1, we take advantage of the plane-wave representation of the Dirac delta function and rewrite the equation as

$$\widehat{B}_{\ell=0}(k_1, k_2, k_3) = \frac{1}{V_B}\int \frac{\mathrm{d}^3x}{(2\pi)^3}\int_{k_1}\mathrm{d}^3q_1\int_{k_2}\mathrm{d}^3q_2\int_{k_3}\mathrm{d}^3q_3\ \delta(\boldsymbol{q}_1)\ \delta(\boldsymbol{q}_2)\ \delta(\boldsymbol{q}_3)\ e^{i\boldsymbol{q}_{123}\cdot\boldsymbol{x}} - B^{\mathrm{SN}}_{\ell=0} \tag{5}$$

$$= \frac{1}{V_B}\int \frac{\mathrm{d}^3x}{(2\pi)^3}\prod_{i=1}^{3} I_{k_i}(\boldsymbol{x}) - B^{\mathrm{SN}}_{\ell=0} \tag{6}$$

where

$$I_{k_i}(\boldsymbol{x}) = \int_{k}\mathrm{d}^3q\ \delta(\boldsymbol{q})\ e^{i\boldsymbol{q}\cdot\boldsymbol{x}}. \tag{7}$$

At this point, we measure $\widehat{B}_{\ell=0}(k_1, k_2, k_3)$ by calcuating the I_{k_i}s with inverse FFTs and summing over in real space.[2] For $\widehat{B}_{\ell=0}$ measurements throughout the paper, we use $\delta(\boldsymbol{x})$ grids with $N_{\rm grid} = 360$ and triangle configurations defined by k_1, k_2, k_3 bins of width $\Delta k = 3k_f = 0.01885\ h/{\rm Mpc}$, three times the fundamental mode $k_f = 2\pi/(1000\ h/{\rm Mpc})$ given the box size.

We present the redshift-space halo bispectrum of the HADE simulations measured using the estimator above in two ways: one that emphasizes the triangle shape dependence (Figure 2) and the other that emphasizes the amplitude (Figure 3). In Figure 2, we plot $\widehat{B}_0(k_1, k_2, k_3)$ as a function of k_2/k_1 and k_3/k_1, which describe the triangle configuration shape. In each panel, the colormap in each (k_2/k_1, k_3/k_1) bin is the weighted average $\widehat{B}_0$ amplitude of all triangle configurations in the bin. The upper left bins contain squeezed triangles ($k_1 = k_2 \gg k_3$); the upper right bins contain equilateral triangles ($k_1 = k_2 = k_3$); and the bottom center bins contain folded triangles ($k_1 = 2k_2 = 2k_3$). We include all possible triangle configurations with $k_1, k_2, k_3 < k_{\rm max} = 0.5\ h/{\rm Mpc}$. The $\widehat{B}_0$ in the upper panels are HADES models with $M_\nu = 0.0$ (fiducial), $0.06, 0.10$, and $0.15\,{\rm eV}$; $\widehat{B}_0$ in the lower panels are HADES models with $M_\nu 0.0$ eV and $\sigma_8 = 0.822, 0.818$, and 0.807. The top and bottom panels of the three right-most columns have matching σ_8 values (Section 2).

Next, in Figure 3, we plot $\widehat{B}_0(k_1, k_2, k_3)$ for all possible triangle configurations with $k_1, k_2, k_3 < k_{\rm max} = 0.5\ h/{\rm Mpc}$ where we order the configurations by looping through k_3 in the inner most loop and k_1 in the outer most loop with $k_1 \leq k_2 \leq k_3$. In the top panel, we present $\widehat{B}_0$ of HADES models with $M_\nu = 0.0, 0.06, 0.10$, and $0.15\,{\rm eV}$; in the lower panel, we present $\widehat{B}_0$ of HADES models with $M_\nu 0.0$ eV and $\sigma_8 = 0.822, 0.818$, and 0.807. We zoom into triangle configurations with $k_1 = 0.113$, $0.226 \leq k_2 \leq 0.283$, and $0.283 \leq k_3 \leq 0.377\ h/{\rm Mpc}$ in the insets of the panels.

4. RESULTS

4.1. *Breaking the M_ν– σ_8 degeneracy*

One major bottleneck of constraining M_ν with the power spectrum alone is the strong $M_\nu - \sigma_8$ degeneracy. The imprint of M_ν and σ_8 on the power spectrum are degenerate and for models with the same σ_8^c, the power spectrum only differ by $< 1\%$ (see Figure 1 and Villaescusa-Navarro et al. 2018). The HADES suite, which has simulations with $M_\nu = 0.0, 0.06, 0.10$, and 0.15 eV as well as $M_\nu = 0.0$ eV simulations with matching σ_8^c — σ_8= 0.822, 0.818, and 0.807 , provide an ideal set of simulations to separate the impact of $M_\nu > 0.0$ eV and examine the degeneracy between M_ν and σ_8 (Section 2 and Table 1). Hence, by measuring bispectrum of these simulations (Figure 2 and 3), we can determine whether the bispectrum helps break the $M_\nu - \sigma_8$ degeneracy. Below, we present our comparison of the HADES bispectrum and illustrate that the bispectrum can significantly improve M_ν constraints by breaking the $M_\nu - \sigma_8$ degeneracy.

We begin by examining the triangle shape dependent imprint of M_ν on the redshift-space halo bispectrum versus σ_8 alone. In Figure 4, we present the fractional residual, $(\Delta\widehat{B}_0 = \widehat{B}_0 - \widehat{B}_0^{\rm fid})/\widehat{B}_0^{\rm fid}$, as a function of k_2/k_1 and k_3/k_1 for $M_\nu = 0.06, 0.10$, and 0.15 eV in the upper panels and 0.0 eV σ_8= 0.822, 0.818, and 0.807 in the bottom panels. The simulations in the top and bottom panels

[2] The code that we use to evaluate $\widehat{B}_{\ell=0}$ is publicly available at https://github.com/changhoonhahn/pySpectrum

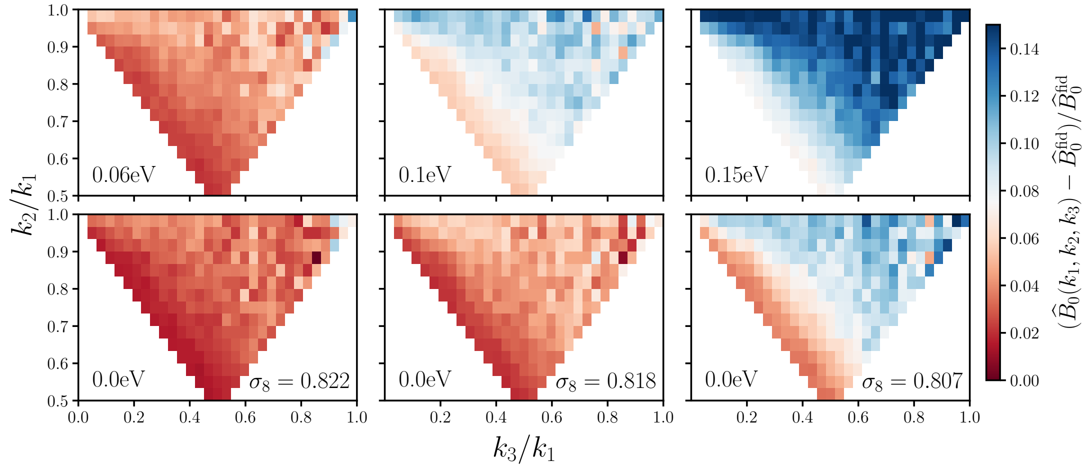

Figure 4. The shape dependence of the M_ν and σ_8 imprint on the redshift-space halo bispectrum, $\Delta\widehat{B}_0/\widehat{B}_0^{\rm fid}$. We align the M_ν= 0.06, 0.10, and 0.15 eV HADES models in the upper panels with M_ν= 0.0 eV σ_8= 0.822, 0.818, and 0.807 models on the bottom such that the top and bottom panels in each column have matching σ_8^c, which produce mostly degenerate imprints on the redshift-space power spectrum. The difference between the top and bottom panels highlight that M_ν leaves a distinct imprint on elongated and isosceles triangles (bins along the bottom left and bottom right edges, respectively) from σ_8. *The imprint of M_ν has an overall distinct shape dependence on the bispectrum that cannot be replicated by varying σ_8.*

of each column have matching σ_8^c. Overall as M_ν increases, the bispectrum increases for all triangle shapes (top panels). This increase is due to halo bias (Villaescusa-Navarro et al. 2018, ; see also Figure 1). We impose a fixed $M_{\rm lim}$ on our halos so lower values of σ_8 translate to a larger halo bias, which boosts the amplitude of the bispectrum. Within the overall increase in amplitude, however, equilateral triangles (upper left) have the largest increase. For $M_\nu = 0.15$ eV, the bispectrum is $\sim 15\%$ higher than $\widehat{B}_0^{\rm fid}$ for equilateral triangles. Meanwhile, the bispectrum increases by $\sim 8\%$ for folded triangles for 0.15 eV (lower center). The noticeable difference in $\Delta\widehat{B}_0/\widehat{B}_0^{\rm fid}$ between equilateral and squeezed triangles (upper left) is roughly consistent with the comparison in Figure 7 of Ruggeri et al. (2018). They, however, fix A_s in their simulations and measure the real-space halo bispectrum so we refrain from any detailed comparisons.

As σ_8 increases, with $M_\nu = 0.0$ eV fixed, the bispectrum increases overall for all triangle shapes (bottom panels). However, the comparison of the top and bottom panels in each column reveals significant differences in $\Delta\widehat{B}_0/\widehat{B}_0^{\rm fid}$ for M_ν versus σ_8 alone. Between $M_\nu = 0.15$ eV and 0.0 eV $\sigma_8 = 0.807$, there is an overall $\gtrsim 5\%$ difference. In addition, the shape dependence of the $\Delta\widehat{B}_0/\widehat{B}_0^{\rm fid}$ increase is different for M_ν than σ_8. This is particularly clear in the differences between 0.1 eV (top center panel) and 0.0 eV and $\sigma_8 = 0.807$ (bottom right panel): near equilateral triangles in the two panels have similar $\Delta\widehat{B}_0/\widehat{B}_0^{\rm fid}$ while triangle shapes near the lower left edge from the squeezed to folded triangles have significantly different $\Delta\widehat{B}_0/\widehat{B}_0^{\rm fid}$. Hence, M_ν leaves an imprint on the bispectrum with a distinct triangle shape dependence than σ_8 alone. In other words, unlike the power spectrum, the triangle shape dependent impact of M_ν on the bispectrum cannot be replicated by varying σ_8.

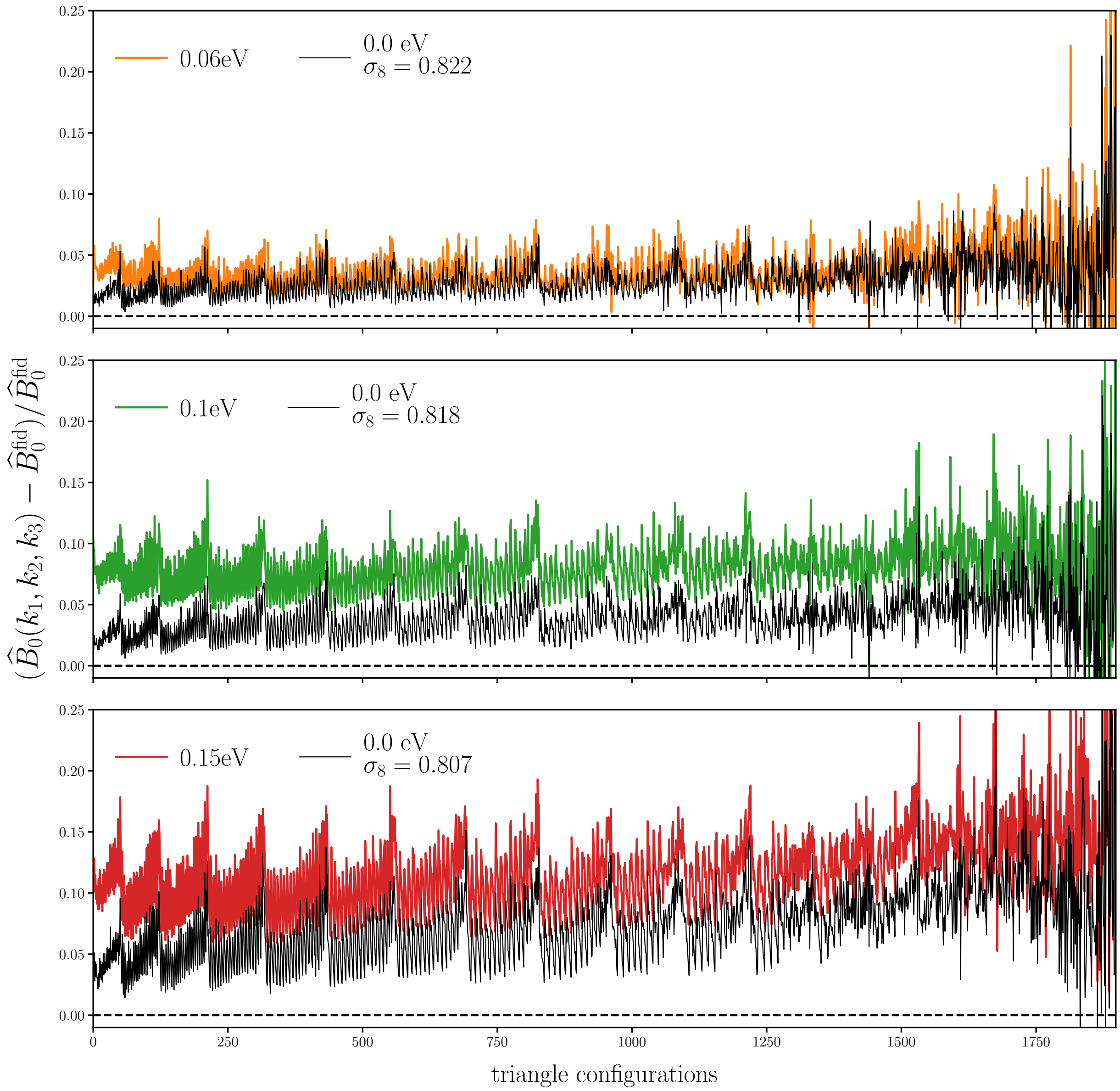

Figure 5. The impact of M_ν and σ_8 on the redshift-space halo bispectrum, $\Delta\widehat{B}_0/\widehat{B}_0^{\rm fid}$, for all 1898 triangle configurations with $k_1, k_2, k_3 \leq 0.5h/{\rm Mpc}$. We compare $\Delta\widehat{B}_0/\widehat{B}_0^{\rm fid}$ of the $M_\nu = 0.06$ (top), 0.10 (middle), and 0.15 eV (bottom) HADES models to $\Delta\widehat{B}_0/\widehat{B}_0^{\rm fid}$ of M_ν= 0.0 eV σ_8= 0.822, 0.818, and 0.807 models. The impact of M_ν on the bispectrum has a significantly different amplitude than the impact of σ_8. For instance, M_ν= 0.15 eV (red) has a $\sim 5\%$ stronger impact on the bispectrum than M_ν= 0.0 eV σ_8= 0.798 (black) even though their powerspectrums only differ by $< 1\%$ (Figure 1). Combined with the different shape-dependence (Figure 4), *the distinct imprint of M_ν on the bispectrum illustrate that the bispectrum can break the degeneracy between M_ν and σ_8 that degrade constraints from two-point analyses.*

We next examine the amplitude of the M_ν imprint on the redshift-space halo bispectrum versus σ_8 alone for all triangle configurations. We present $\Delta\widehat{B}_0/\widehat{B}_0^{\rm fid}$ for all 1898 possible triangle configurations with $k_1, k_2, k_3 < k_{\rm max} = 0.5\ h/{\rm Mpc}$ in Figure 5. We compare $\Delta\widehat{B}_0/\widehat{B}_0^{\rm fid}$ of the $M_\nu = 0.06, 0.10,$ and

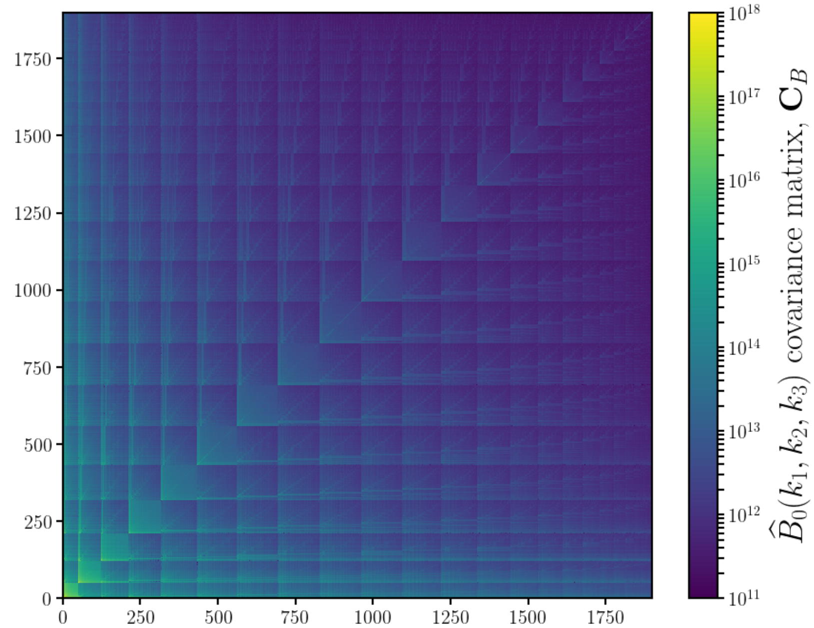

Figure 6. Covariance matrix of the redshift-space halo bispectrum estimated using $N_{\rm cov} = 15,000$ realizations of the Qujiote simulation suite at the fiducial cosmology: $\Omega_{\rm m}$=0.3175, $\Omega_{\rm b}$=0.049, h=0.6711, n_s=0.9624, σ_8=0.834, and M_ν=0.0 eV. We include all possible triangle configurations with $k_1, k_2, k_3 \leq k_{\rm max} = 0.5\,h/{\rm Mpc}$ and order the configurations (bins) in the same way as Figures 3 and 5. We use the covariance matrix above for the Fisher matrix forecasts presented in Section 4.2.

0.15 eV HADES models to the $\Delta\widehat{B}_0/\widehat{B}_0^{\rm fid}$ of M_ν= 0.0 eV σ_8= 0.822, 0.818, and 0.807 models in the top, middle, and bottom panels, respectively. The comparison confirms the difference in overall amplitude of varying M_ν and σ_8 (Figure 4). For instance, M_ν= 0.15 eV (red) has a $\sim 5\%$ stronger impact on the bispectrum than M_ν= 0.0 eV σ_8= 0.798 (black) even though their power spectrums differ by $< 1\%$ (Figure 1).

The comparison in the panels of Figure 5 also reveal a difference in the configuration dependence in $\Delta\widehat{B}_0/\widehat{B}_0^{\rm fid}$ between M_ν versus σ_8. The triangle configurations are ordered by looping through k_3 in the inner most loop and k_1 in the outer most loop such that $k_1 \leq k_2 \leq k_3$. In this ordering, k_1 increases from left to right. $\Delta\widehat{B}_0/\widehat{B}_0^{\rm fid}$ of M_ν expectedly increases with k_1: for small k_1 (on large scales), neutrinos behave like CDM and therefore the impact is reduced. However, $\Delta\widehat{B}_0/\widehat{B}_0^{\rm fid}$ of M_ν has a smaller k_1 dependence than $\Delta\widehat{B}_0/\widehat{B}_0^{\rm fid}$ of σ_8. Combined with the different shape-dependence (Figure 4), the distinct imprint of M_ν on the redshift-space halo bispectrum illustrates that the bispectrum can break the degeneracy between M_ν and σ_8. Moreover it illustrates that by including the bispectrum, we can more precisely constrain M_ν than with the power spectrum alone.

4.2. *M_ν and other Cosmological Parameter Forecasts*

We demonstrate in the previous section with the HADES simulations, that the bispectrum helps break the M_ν–σ_8 degeneracy, a major challenge in precisely constraining M_ν with the power spectrum. This establishes the bispectrum as a promising probe for M_ν. However, we are ultimately interested in determining the constraining power of the bispectrum for an analysis that include cosmological parameters beyond M_ν and σ_8— *i.e.* Ω_m, Ω_b, h, and n_s. The Quijote suite of simulations is *specifically* designed to answer this question through Fisher matrix forecast.

First, the Quijote suite includes $N_\mathrm{cov} = 15,000$ N-body realizations run at a fidicial cosmology: M_ν=0.0eV, Ω_m=0.3175, Ω_b=0.049, n_s=0.9624, h=0.6711, and $\sigma_8 = 0.834$ (see Table 1. This allows us to robustly estimate the covariance matrix of the bispectrum, $\boldsymbol{C}$, which has $\sim$1,800 triangle configurations (Figure 6). Second, the Quijote suite includes 500 N-body realizations evaluated at 13 different cosmologies, each a small step away from the fiducial cosmology parameter values along one parameter (Section 2 and Table 1). On top of this, we apply redshift-space distortions along 3 different directions for these 500 realizations, which then gives us $N_\mathrm{deriv.} = 1,500$ realizations. These realizations allow us to precisely estimate the derivatives of the bispectrum with respect to each of the cosmological parameters.

Since their introduction to cosmology over two decades ago, Fisher Information matrices have been ubiquitously used to forecast the constraining power of future experiments (*e.g.* Jungman et al. 1996; Tegmark et al. 1997; Dodelson 2003; Heavens 2009; Verde 2010). Defined as

$$F_{ij} = -\left\langle \frac{\partial^2 \ln\mathcal{L}}{\partial\theta_i \partial\theta_j} \right\rangle, \tag{8}$$

where $\mathcal{L}$ is the likelihood, the Fisher matrix for the bispectrum can be written as

$$F_{ij} = \frac{1}{2}\,\mathrm{Tr}\left[\boldsymbol{C}^{-1}\frac{\partial \boldsymbol{C}}{\partial\theta_i}\boldsymbol{C}^{-1}\frac{\partial \boldsymbol{C}}{\partial\theta_j} + \boldsymbol{C}^{-1}\left(\frac{\partial\overline{B}_0}{\partial\theta_i}\frac{\partial\overline{B}_0}{\partial\theta_j}^T + \frac{\partial\overline{B}_0}{\partial\theta_i}^T\frac{\partial\overline{B}_0}{\partial\theta_j}\right)\right]. \tag{9}$$

Since we assume that the B_0 likelihood is Gaussian, including the first term in Eq. 9 runs the risk of incorrectly including information from the covariance already included in the mean (Carron 2013). We, therefore, conservatively neglect the first term and calculate the Fisher matrix,

$$F_{ij} = \frac{1}{2}\,\mathrm{Tr}\left[\boldsymbol{C}^{-1}\left(\frac{\partial\overline{B}_0}{\partial\theta_i}\frac{\partial\overline{B}_0}{\partial\theta_j}^T + \frac{\partial\overline{B}_0}{\partial\theta_i}^T\frac{\partial\overline{B}_0}{\partial\theta_j}\right)\right], \tag{10}$$

directly with $\boldsymbol{C}$ and $\partial B_0/\partial\theta_i$ along each cosmological parameter from the Quijote simulations.

For Ω_m, Ω_b, h, n_s, and σ_8, we estimate

$$\frac{\partial\overline{B}_0}{\partial\theta_i} \approx \frac{\overline{B}_0(\theta_i^+) - \overline{B}_0(\theta_i^-)}{\theta_i^+ - \theta_i^-}, \tag{11}$$

where $\overline{B}_0(\theta_i^+)$ and $\overline{B}_0(\theta_i^-)$ are the average bispectrum of the 1,500 realizations at θ^+ and θ^-. Meanwhile, for M_ν, where the fiducial value is 0.0 eV and we cannot have negative M_ν, we use the Quijote simulations at M_ν^+, M_ν^{++}, $M_\nu^{+++} = 0.1, 0.2, 0.4$ eV (Table 1) to estimate

$$\frac{\partial\overline{B}_0}{\partial M_\nu} \approx \frac{-21\overline{B}_0(M_\nu^\mathrm{fid}) + 32\overline{B}_0(M_\nu^+) - 12\overline{B}_0(M_\nu^{++}) + \overline{B}_0(M_\nu^{+++})}{1.2}, \tag{12}$$

which provides a $\mathcal{O}(\delta M_\nu^2)$ order approximation. By using these N-body simulations, instead of analytic methods (*e.g.* perturbation theory), we exploit the accuracy of numerical simulations in the

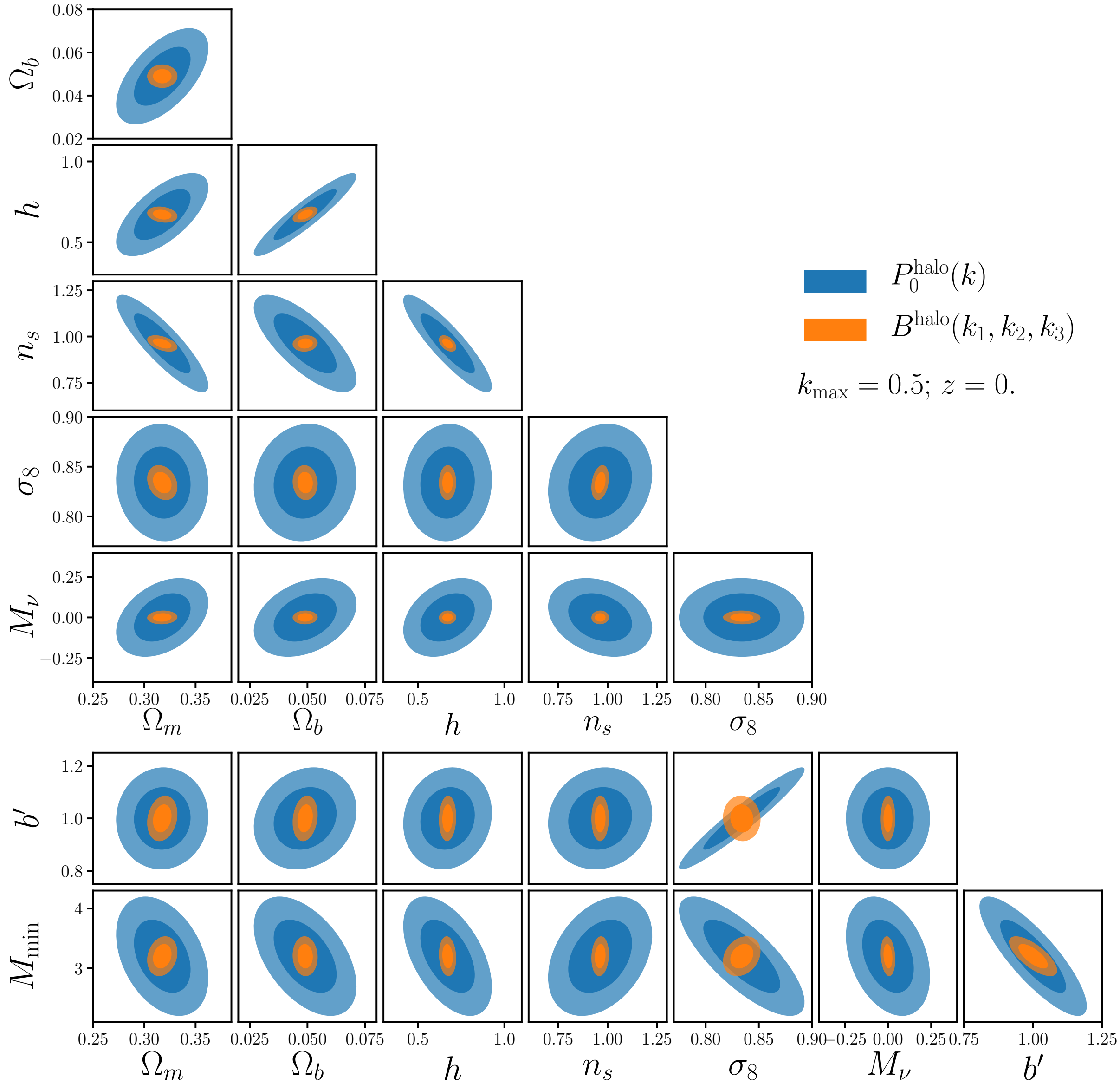

Figure 7. Fisher matrix constraints for M_ν and other cosmological parameters for the redshift-space halo bispectrum monopole (orange). We include Fisher parameter constraints for the redshift-space halo power-spectrum monopole in blue for comparison. The contours mark the 68% and 95% confidence interals. We set $k_{\rm max} = 0.5\ h/{\rm Mpc}$ for both power spectrum and bispectrum. We include in our forecasts b' and $M_{\rm min}$, a free amplitude scaling factor and halo mass limit, respectively. They serve as a simplistic bias model and we marginalize over them so that our constraints do not include extra constraining power from the difference in bias/number density in the different Quijote cosmologies. The bispectrum *substantially* improves constraints on all of the cosmological parameters over the power spectrum. Constraints on $\Omega_{\rm m}$, $\Omega_{\rm b}$, h, n_s, and σ_8 improve by factors of 3.1, 4.1, 5.1, 5.9, and 3.3, respectively. *For M_ν, the bispectrum improves σ_{M_ν} from 0.1962 to 0.0342 eV — a factor of ∼6 improvement over the power spectrum.*

nonlinear regime and rely on fewer assumptions and approximations. In fact, *these N-body simulation estimated derivatives are the key ingredients that enables us to quantify, for the first time, the full information content of the redshift-space bispectrum in the non-linear regime*. We discuss subtleties of Eq. 12 bispectrum derivative and tests of convegence in Appendix B.

We present the constraints on M_ν and other cosmological parameters $\{\Omega_\mathrm{m}, \Omega_\mathrm{b}, h, n_s, \sigma_8\}$ derived from the redshift-space halo bispectrum Fisher matrix (Eq. 10) for $k_\mathrm{max} = 0.5\ h/\mathrm{Mpc}$ in Figure 7, respectively. We include Fisher constraints for the redshift-space halo power spectrum monopole with the same k_max for comparison (blue). We mark the 68% and 95% confidence interals with the contours. We include in our Fisher constraints the following nuisance parameters: b', a scaling factor on the bispectrum amplitude, and M_min, the halo mass limit. b' is analogous to linear bias. Meanwhile, we choose M_min as a nuisance parameter to address the difference in the number densities among the Quijote cosmologies, which impacts the derivatives $\partial\overline{B}_0/\partial\theta_i$. For instance, the σ_8^+ and σ_8^- cosmologies have halo $\bar{n} = 1.586\times10^{-4}$ and $1.528\times10^{-4}(h^{-1}\mathrm{Mpc})^3$. These parameters serve as a simplistic bias model and by marginalizing over them we aim to ensure that our Fisher constraints do not include extra constraining power from the difference in bias or number density. b' is a multiplicative factor so $\partial\overline{B}_0/\partial b' = \overline{B}_0$. Meanwhile, we numerically estimate $\partial\overline{B}_0/\partial M_\mathrm{min}$ using $\overline{B}_0$ evaluated at M^+_min=$3.3\times10^{13}h^{-1}M_\odot$ and M^-_min=$3.1\times10^{13}h^{-1}M_\odot$, with all other parameters set to the fiducial value.

The bispectrum *substantially* improves constraints on all parameters over the power spectrum. For $k_\mathrm{max} = 0.5\ h/\mathrm{Mpc}$, the bispectrum improves the marginalized constraints, σ_θ of Ω_m, Ω_b, h, n_s, and σ_8 by factors of ~3, 4, 5, 6, and 3 over the power spectrum. *For M_ν, the bispectrum improves the constraint from σ_{M_ν}= 0.1962 to 0.0342eV — a factor of 6 improvement over the power spectrum.* We emphasize that this σ_{M_ν}=0.0342eV constraint is for the *bispectrum alone* and only for a $1h^{-1}$Gpc box. We list the precise marginalized Fisher parameter constraints of both cosmological and nuisance parameters for P_0 and B_0 in Table 2.

Even below $k_\mathrm{max} < 0.5\ h/\mathrm{Mpc}$, the bispectrum significantly improves cosmological parameter constraints. We compare σ_θ, the marginalized 1σ constraints of Ω_m, Ω_b, h, n_s, σ_8, and M_ν, as a function of k_max for B_0 (orange) and P_0 (blue) in Figure 8. We focus only on the k_max range where the Fisher forecast is well defined — *i.e.* more data bins than the number of parameters: $k_\mathrm{max} > 8k_\mathrm{f} \approx 0.05\ h/\mathrm{Mpc}$ for P_0 and $k_\mathrm{max} > 12k_\mathrm{f} \approx 0.075\ h/\mathrm{Mpc}$ for B_0. Figure 8 reveals that the improvement of the bispectrum σ_θ over the power spectrum σ_θ is larger at higher k_max. Although limited by the k_max range, the figure suggests that on large scales ($k_\mathrm{max} \lesssim 0.1\ h/\mathrm{Mpc}$) P_0 σ_θ crosses over B_0 σ_θ so P_0 has more constraining power than B_0— as expected on linear scales. On slightly larger k_max, even at $k_\mathrm{max} = 0.2\ h/\mathrm{Mpc}$, we find that the bispectrum substantially improves σ_θ by factors of $\sim$ 1.8, 2.1, 2.6, 2.5, 2.6, and 3.1 for Ω_m, Ω_b, h, n_s, σ_8, and M_ν respectively.

Our forecasts demonstrate that the bispectrum has significant constraining power in the weakly non-linear regime ($k > 0.1\ h/\mathrm{Mpc}$) beyond the power spectrum. This constraining power comes from the bispectrum breaking degeneracies among the cosmological and nuisance parameters. This is evident when we compare the unmarginalized constraints from P_0 and B_0: $1/\sqrt{F_{ii}}$, where F_{ii} is a diagonal element of the Fisher matrix. For $k < 0.4\ h/\mathrm{Mpc}$, the unmarginalized cosntraints from P_0

Table 2. Marginalized Fisher parameter constraints from the redshift-space halo power spectrum (top) and bispectrum (bottom) for different values of $k_{\rm max}$. We list constraints for cosmological parameters M_ν, Ω_m, Ω_b, h, n_s, and σ_8 as well as nuisance parameters b' and $M_{\rm min}$

	$k_{\rm max}$ (h/Mpc)	M_ν (eV)	Ω_m	Ω_b	h	n_s	σ_8	b'	$M_{\rm min}$ ($10^{13}h^{-1}M_\odot$)
		0.0	0.3175	0.049	0.6711	0.9624	0.834	1.	3.2
P_0	0.2	0.333	±0.052	±0.030	±0.372	±0.347	±0.128	±0.649	±5.045
	0.3	0.277	±0.044	±0.023	±0.273	±0.276	±0.069	±0.383	±2.457
	0.4	0.228	±0.040	±0.020	±0.235	±0.240	±0.059	±0.226	±1.270
	0.5	±**0.196**	±0.036	±0.018	±0.207	±0.213	±0.048	±0.157	±0.807
B_0	0.2	0.107	±0.029	±0.014	±0.144	±0.140	±0.050	±0.265	±1.317
	0.3	0.065	±0.020	±0.008	±0.077	±0.074	±0.023	±0.143	±0.657
	0.4	0.043	±0.015	±0.006	±0.052	±0.047	±0.016	±0.088	±0.369
	0.5	±**0.034**	±0.012	±0.004	±0.040	±0.036	±0.014	±0.070	±0.269

are tighter than those from B_0. Yet, once we marginalize the constraints over the other parameters, the B_0 constraints are tigher than P_0 for $k > 0.1\ h/{\rm Mpc}$. The derivatives, $\partial B_0/\partial\theta_i$, also shed light on how B_0 breaks parameter degeneracies. The parameter degeneracies in the P_0 forecasts of Figure 7 are consistent with similarities among the shape and scale dependence of P_0 derivatives $\partial P_0/\partial\theta$. On the other hand, the B_0 derivatives with respect to the parameters have significant different scale and triangle shape dependences. **CH:** derivative figure?

By exploiting the unprecedented number of N-body simulations of the Quijote suite, we present for the first time the full information content of the redshift-space bispectrum beyond the linear regime. The information content of the bispectrum, however, has previously been examined using perturbation theory. Previous works, for instance, measure the signal-to-noise ratio (SNR) of the bispectrum derived from covariance matrices estimated using perturbation theory (*e.g.* Sefusatti & Scoccimarro 2005; Chan & Blot 2017). Most recently, Chan & Blot (2017), using covariance matrices that include non-Gaussian contributions calibrated with N-body simulations, find that the cumulative SNR of the halo bispectrum is $\sim 30\%$ of the SNR of the halo power spectrum at $k_{\rm max} \sim 0.1\ h/{\rm Mpc}$ and increases to $\sim 40\%$ at $k_{\rm max} \sim 0.35\ h/{\rm Mpc}$. While these simple SNR measurements cannot be easily compared to our Fisher analysis, we note that they are loosely consistent with the unmarginalized constraints, where we find tighter unmarginalized constraints from P_0 than B_0 at $k_{\rm max} < 0.4\ h/{\rm Mpc}$. Also, when we measure the the halo power spectrum and bispectrum SNRs using our covariance matrices (Figure 6), we find a relation between the SNRs consistent with Chan & Blot (2017). Beyond the k range of Chan & Blot (2017) ($k_{\rm max} > 0.35\ h/{\rm Mpc}$), we find that the SNR of B_0 continues to increase at higher $k_{\rm max}$ in constract to the P_0 SNR, which saturates at $k_{\rm max} \sim 0.1\ h/{\rm Mpc}$. At $k_{\rm max} = 0.75\ h/{\rm Mpc}$, the largest k we probe, the B_0 SNR is $\sim 75\%$ of the P_0 SNR.

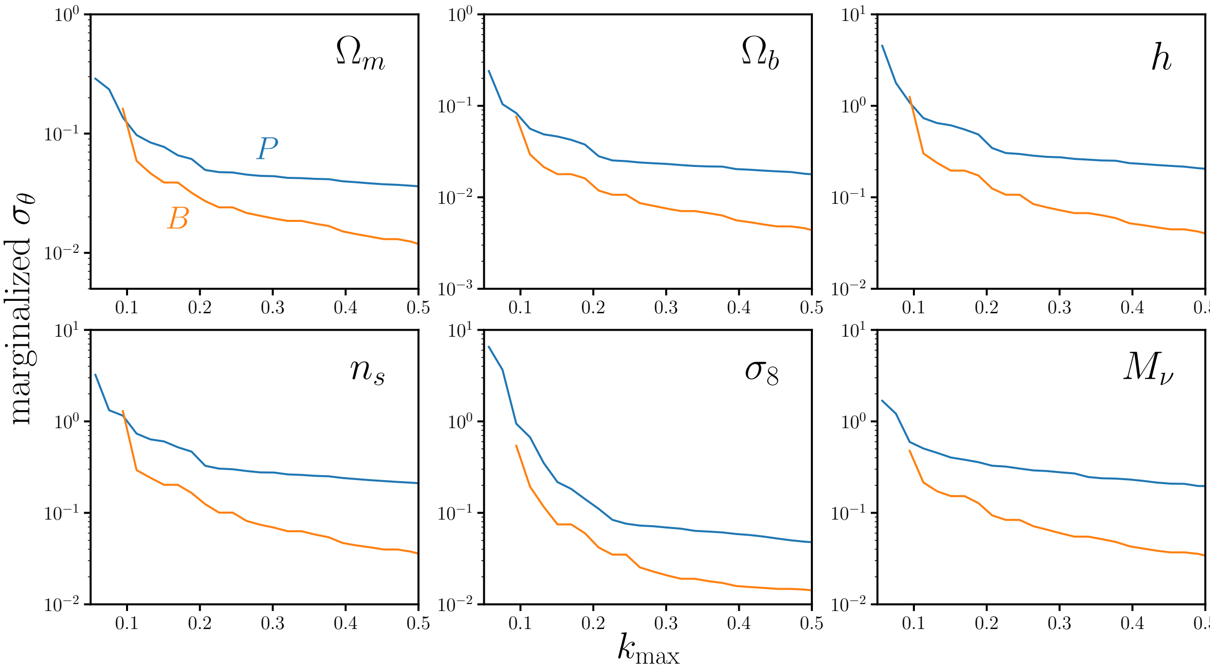

Figure 8. Marginalized 1σ constraints of the cosmological parameters $\Omega_{\rm m}$, $\Omega_{\rm b}$, h, n_s, σ_8, and M_ν (σ_θ) as a function of $k_{\rm max}$ for the redshift-space halo bispectrum (orange) and power spectrum (blue). Though not included in the figure, we marginalize over the nuisance parameters b' and $M_{\rm min}$ in our forecast (Section 4.2). We only include $k_{\rm max} > 8k_{\rm f}$ for P_0 and $k_{\rm max} > 12k_{\rm f}$ for B_0 — $k_{\rm max}$ ranges where we have more data bins than number of parameters. Even at $k_{\rm max} < 0.5\ h/{\rm Mpc}$, the bispectrum significantly improves cosmological parameter constraints. The improvement, however, is larger for higher $k_{\rm max}$. At $k_{\rm max} = 0.2\ h/{\rm Mpc}$, the bispectrum improves constraints on $\Omega_{\rm m}$, $\Omega_{\rm b}$, h, n_s, σ_8, and M_ν by factors of ~ 1.8, 2.1, 2.6, 2.5, 2.6, and 3.1 over the power spectrum.

Beyond these signal-to-noise calculations, a number of previous works quantify the information content of the bispectrum with Fisher forecasts (Scoccimarro et al. 2004; Sefusatti et al. 2006; Sefusatti & Komatsu 2007; Song et al. 2015; Tellarini et al. 2016; Yamauchi et al. 2017; Karagiannis et al. 2018; Yankelevich & Porciani 2019). While most of these works fix most cosmological parameters and focus soley on forecasting constraints of primordial non-Gaussianity ($f_{\rm NL}$) and bias parameters, Sefusatti et al. (2006) and Yankelevich & Porciani (2019) provide bispectrum forecasts for full sets of cosmological parameters. In Sefusatti et al. (2006), they present likelihood analysis forecasts for ω_d, ω_b, Ω_Λ, n_s, A_s, w, τ. For ΛCDM, with fixed bias parameters, and $k_{\rm max} = 0.3\ h/{\rm Mpc}$, they find constraints on $\Omega_{\rm m}$, $\Omega_{\rm b}$, h, n_s, and σ_8 from WMAP, P_0, and B_0 is a factor of 1.71, 1.3, 1.4, 1.2, and 1.5 tighter than constraints from WMAP and P_0 alone. In comparison, for $k_{\rm max} = 0.3\ h/{\rm Mpc}$ our B_0 constraints are tighter than P_0 constraints by factors of 2.1, 2.9, 3.5, 3.7, and 3.0. Both Sefusatti et al. (2006) and our analysis find significantly tighter constraints with the bispectrum. They however include the WMAP likelihood in their forecast and only present constraints with both P_0 and B_0. We also emphasize that they use perturbation theory bispectrum models, which break down on small scales. In a comparison with N-body simulations, **?** find that perturbation theory models of the matter bispectrum deviate by $> 5\%$ at $k_{\rm max} \gtrsim 0.15\ h/{\rm Mpc}$.

Meanwhile, in Yankelevich & Porciani (2019), they present Fisher forecasts for $\Omega_{\rm cdm}$, $\Omega_{\rm b}$, h, n_s, A_s, w_0, and w_0 for a Euclid-like survey (**?**) in 14 non-overlapping redshift bins over $0.65 < z < 2.05$. They use the full redshift-space bispectrum, rather than just the monopole, and a more sophisticated bias expansion than Sefusatti et al. (2006) that depend on the tidal field. They use a pertrubative model for the bispectrum, which consequently limit their forecast to $k_{\rm max} = 0.15\ h/{\rm Mpc}$. From their forecasts, they find similar constraining power on cosmological parameters from B alone as P. They also find that combining the bispectrum with the power spectrum only moderately improves parameter constraints because posterior correlations are similar for P and B. While this seemingly conflicts with the results we present, there are significant differences between our forecasts. For instance, their forecasts are at higher redshifts, $z > 0.7$, where we expect the constraining power of B to be weaker than at $z = 0$. They also forecast the *galaxy* P and B and marginalizes over 56 nuisance parameters (14 z bins each with 3 bias parameters and 1 RSD parameter). They also neglect non-Gaussian contributions to the B covariance matrix, which substantially impact the constraints especially on small scales (Chan & Blot 2017). Despite differences, Yankelevich & Porciani (2019) find that the constraining power of B relative to P increases for higher $k_{\rm max}$, consistent with our forecasts as a function of $k_{\rm max}$ (Figure **??**). Also, similar to their forecast, for for $k_{\rm max} = 0.15\ h/{\rm Mpc}$, we also find similar posterior correlations between the P_0 and B_0 constraints. At $k_{\rm max} = 0.5\ h/{\rm Mpc}$, however, we find significantly less correlations (Figure 7). Based on our forecasts, at higher $k_{\rm max}$ adding B_0 to the analysis improve parameter constraints beyond the improvement found in Yankelevich & Porciani (2019).

While the various difference between our forecast and previous work prevent more thorough comparisons, the main difference is that we present the first bispectrum forecasts for a full set of cosmological parameters using bispectrum measurements entirely from N-body simulations. This allows us to go beyond previous perturbation theory based forecasts and quantify the full information content of the redshift-space bispectrum all the way out to the non-linear regime. Moreover, we also present the first bispectrum forecast of cosmological parameters including neutrinos and demonstrate the potential of the bispectrum in constraining M_ν. Below, we underline a few caveats of our Fisher forecasts.

First, the parameter constraints were derived using the Fisher matrix. This assumes

Q: How robust are Fisher forecasts

A: There are many caveats to the Fisher forecast. One of the main limitation is that Fisher forecasts assume the posteriors are Gaussian, this can result in incorrect posteriors Wolz et al. (2012). Convergence of the covariance matrix and derivatives are also key. We discuss this in the appendix and they do not seem to be an issue.

Q: A lot of the advantages from breaking parameter degeneracies. How robust is this?

A: We address this by imposing Planck priors on our forecasts. This expectedly has a large impact on P constraints, but doesn't change B constraints much. B still does better by a lot. This suggests that the breaking of parameter degeneracies are relatively stable to poorly constrained derivatives spuriously breaking degeneracies so this is robust. Also demonstrates that the gains are relatively stable to Fisher forecasts caveats (i.e. projecting a banana).

Another caveat is that our parameter constraints were derived using the power spectrum and bispectrum of halo in a periodic box. We do not consider a realistic survey geometry or radial selection function. A realistic selection function will smooth out the triangle configuration dependence and consequently degrade the constraining power of the bispectrum. In Sefusatti & Scoccimarro (2005), for instance, they find that the signal-to-noise of the bispectrum is significantly reduced once survey geometry is included in their forecast. Survey geometry, however, also degrade the signal-to-noise of their power spectrum forecasts. Hence, with the order of magnitude improve in the M_ν constraining power of the bispectrum, even with survey geometry, including the bispectrum will improve M_ν constraints.

Q: extra information leaking in due to non-linear bias and number density differences?
A: We ran tests that include SN correction parameters in case number density information is leaking in from there. Constraints barely change. We also include and marginalize over b_2 and g_2 but nothing changes. Explain fixed nbar tests that we ran, which also came out short. Talk about how these tests don't definitely answer whether non-linear bias information is leaking into the forecasts since b', $M_{\rm min}$, b_2, and g_2 may not a sufficient model of halo bias. We suspect this is the reason why B does better than P for all $k_{\rm max}$ even though on linear scales we expect P to have more constraining power. However since the ultimate goal is to constrain M_ν with the galaxy bispectrum. For galaxy bispectrum, HOD is a more robust bias model. The halo bispectrum is an intermediate step and a proof of concept, which our results show is promising. We therefore refrain from an exhaustive investigation of halo bias and go directly to HOD in the next paper of this series.

Although we focus on the halo bispectrum and power spectrum in this paper, constraints on M_ν will ultimately be derived from the distribution of galaxies. Besides the cosmological parameters, bias and nuisance parameters that allow us to marginalize over the galaxy—halo connection need to be incorporated to forecast M_ν and other cosmological parameter constraints for the galaxy bispectrum. Although we include a *naive* bias model through b' and $M_{\rm min}$, this is insufficient to describe how galaxies occupy halos. A more realistic bias model such as a halo occupation distribution (HOD) model involve extra parameters that describe the distribution of central and satellite galaxies in halos (*e.g.* Zheng et al. 2005; Leauthaud et al. 2012; Tinker et al. 2013; Zentner et al. 2016; Vakili & Hahn 2019). **CH:** maybe something about Uros and Nick's model involving a lot of parameters. Marginalizing over these extra parameters, will likely reduce the constraining power at high k. Even if the constraining power at high k is reduced, the bispectrum still offers significant improvements over the power spectrum at $k_{\rm max} \sim 0.2$. Jointly analyzing power spectrum and bispectrum will help constrain these extra bias parameters. **CH:** talk about Yankelevich & Porciani (2019) how they don't find as much of an improvement for the galaxy bispectrum alone. But they do find that jointly analyzing P and B improve results significantly. Don't read too into this because of all the differences that we mentioned. Furthermore, we again emphasize that the constraints we present in this paper is for a $1h^{-1}$Gpc box. In Hahn et al. (in preparation), we will include a realistic HOD model and quantify

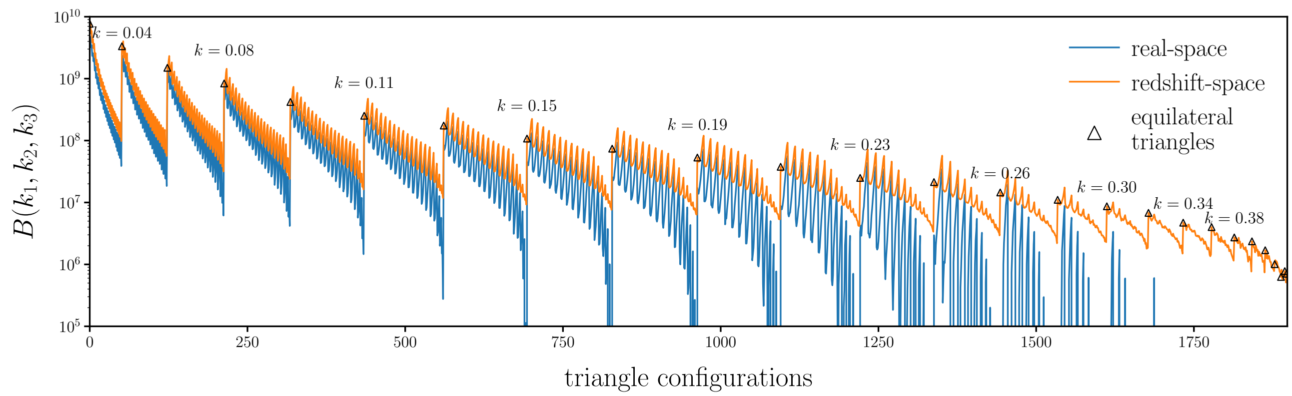

Figure 9. Comparison of the fiducial HADES simuluations real and redshift-space halo bispectrum for triangle configurations with $k_1, k_2, k_3 \leq k_{\rm max} = 0.5h/{\rm Mpc}$ (blue and orange respectively). We mark equilateral triangle configurations (empty triangle marker) along with their side lengths k.

the information content and constraining power of a joint galaxy power spectrum and bispectrum analysis.

5. SUMMARY

CH: talk about DESI, PFS, WFIRST

ACKNOWLEDGEMENTS

It's a pleasure to thank Enea Di Dio, Daniel Eisenstein, Simone Ferraro, Shirley Ho, Emmaneul Schaan, Zachary Slepian, David N. Spergel, and Benjamin D. Wandelt for valuable discussions and comments.

APPENDIX

A. REDSHIFT-SPACE HALO BISPECTRUM

CH: do we want to keep this section?

B. FISHER FORECASTS USING N-BODY SIMULATIONS

The two key elements in calculating the Fisher matrices we use in our forecasts are the bispectrum covariance matrix ($\boldsymbol{C}$; Figure 6) and the derivatives of the bispectrum along the cosmological and nuisance parameters, $\partial B_0/\partial\theta_i$ (Section 4.2). We compute both these elements directly using the N-body simulations of the Quijote suite (Section 2). This takes advantage of the N-body simulations and allows us to accurately quantify the constraining power of the bispectrum that come from the nonlinear regime. However, to trust our forecast, we must ensure that both $\boldsymbol{C}$ has converged and that the numerically calculated $\partial B_0/\partial\theta_i$ do not introduce any biases. Below, we tests the convergence of $\boldsymbol{C}$ and $\partial B_0/\partial\theta_i$ and discuss some of the subtleties and caveats of numerically calculating $\partial B_0/\partial\theta_i$ from the Quijote simulations. **CH:** mention somewhere the P convergence looks good

To estimate $\boldsymbol{C}$, we use 15,000 Quijote N-body simulations at the fiducial cosmology. This is a *significantly* larger number of simulations than previous bispectrum analyses; however, we also consider a larger number of triangle configurations — 1898 triangles out to $k_{\rm max} = 0.5\ h/{\rm Mpc}$. For reference, the recent Gil-Marín et al. (2017) analysis used 2048 simulations to estimate the covariance matrix of the bispectrum with 825 configurations. We, therefore, check the convergence of $\boldsymbol{C}$ by varying $N_{\rm fid}$, the number of simulations used to estimate $\boldsymbol{C}$, and examining whether this significantly impacts the Fisher parameter constraints. We present $\sigma_\theta(N_{\rm fid})/\sigma_\theta(N_{\rm fid} = 15,000)$, the ratio of the 1σ Fisher constraint for $\theta = \Omega_{\rm m}$, $\Omega_{\rm b}$, h, n_s, σ_8, and M_ν calculated with $N_{\rm fid}$ over the constraint calculated with $N_{\rm fid} = 15,000$, as a function of $N_{\rm fid}$ (Figure 10 left panel). The 1σ Fisher constraints on the parameters vary by $< 10\%$ for $N_{\rm fid} > 7000$; in fact, the constraints vary by $< 1\%$ for $N_{\rm fid} > 14,000$. Hence, we conclude that we have a sufficient number of simulations to estimate the bispectrum $\boldsymbol{C}$ and our forecasts are robust to the convergence of $\boldsymbol{C}$.

We estimate $\partial B_0/\partial\theta_i$ numerically using 13 sets of $N_{\rm fp} = 500$ fixed paired simulations (Table 1). To check the convergence of $\partial B_0/\partial\theta_i$ and its impact on our forecast we present the ratio of the 1σ Fisher constraint for θ calculated using $N_{\rm fp}$ simulations over the constraint calculated with $N_{\rm fp} = 500$, $\sigma_\theta(N_{\rm fp})/\sigma_\theta(N_{\rm fp} = 500)$, as a function of $N_{\rm fp}$ (Figure 10 right panel). Unlike $\sigma_\theta(N_{\rm fid})$, $\sigma_\theta(N_{\rm fp})$ depend significantly on θ. For instance, σ_θ for σ_8 and $\Omega_{\rm m}$ vary by $< 10\%$ for $N_{\rm fp} > 300$ and $< 2\%$ for $N_{\rm fp} > 450$. σ_θ for the other parameter vary significantly more. Nonetheless, for $N_{\rm fp} > 400$ and 450 they vary by < 10 and 5%, respectively.

For $\Omega_{\rm m}$, $\Omega_{\rm b}$, h, n_s, σ_8, and $M_{\rm lim}$ we estimate $\partial B_0/\partial\theta_i$ using a centered difference approximation (Eq. 11). However, for M_ν, where we cannot have values below 0.0 eV, we cannot estimate the derivative with the same method. If we use the forward difference approximation,

$$\frac{\partial \overline{B}_0}{\partial M_\nu} \approx \frac{\overline{B}_0(M_\nu^{\rm fid} + \delta M_\nu) - \overline{B}_0(M_\nu^{\rm fid})}{\delta M_\nu}, \tag{B1}$$

the error goes as $\mathcal{O}(\delta M_\nu)$. Instead, we use Eq. 12, which provides a $\mathcal{O}(\delta M_\nu^2)$ order approximation. In our $\partial B_0/\partial M_\nu$ approximation, we use the Quijote simulations at M_ν^{+}, M_ν^{++}, and M_ν^{+++}. We compare $\partial \log B(k_1, k_2, k_3)/\partial M_\nu$ (right) and $\partial \log P(k)/\partial M_\nu$ (left), computed using Eq. 12 (blue) and the forward difference approximation (green) in Figure 11. We also include P and B derivatives approximated using only the M_ν^{+} and M_ν^{++} simulations in orange. **CH:** update numbers: The three approximations for the derivatives differ from one another by roughly 10% with Eq. 12 producing the largest estimate for both P_0 and B_0. If we use the M_ν^{+} and M_ν^{++} and forward difference derivatives instead of the Eq. 12 for our Fisher forecasts, we find the following marginalized M_ν constraints for $k_{\rm max} = 0.5\ h/{\rm Mpc}$: 0.196 and 0.294eV for P_0 and 0.0308 and 0.0483eV for B_0. These correspond to a ~ 20 and 80% relative increase from our forecasts in Section 4.2. The forward difference derivatives have a significant impact on our forecasts; however, we emphasize that this is a $\mathcal{O}(\delta M_\nu)$ approximation, unlike the other $\mathcal{O}(\delta M_\nu^2)$ approximations. Moreover, because the discrepancies in the derivative propogate similarly to the P_0 and B_0 constraints, the relative improvement of B_0 over P_0 remains roughly the same. Hence we conclude that the derivatives have sufficiently converged and robust for our Fisher forecasts.

REFERENCES

Ade, P. a. R., Aghanim, N., Arnaud, M., et al. 2016, Astronomy & Astrophysics, 594, A13

Angulo, R. E., & Pontzen, A. 2016, Monthly Notices of the Royal Astronomical Society, 462, L1

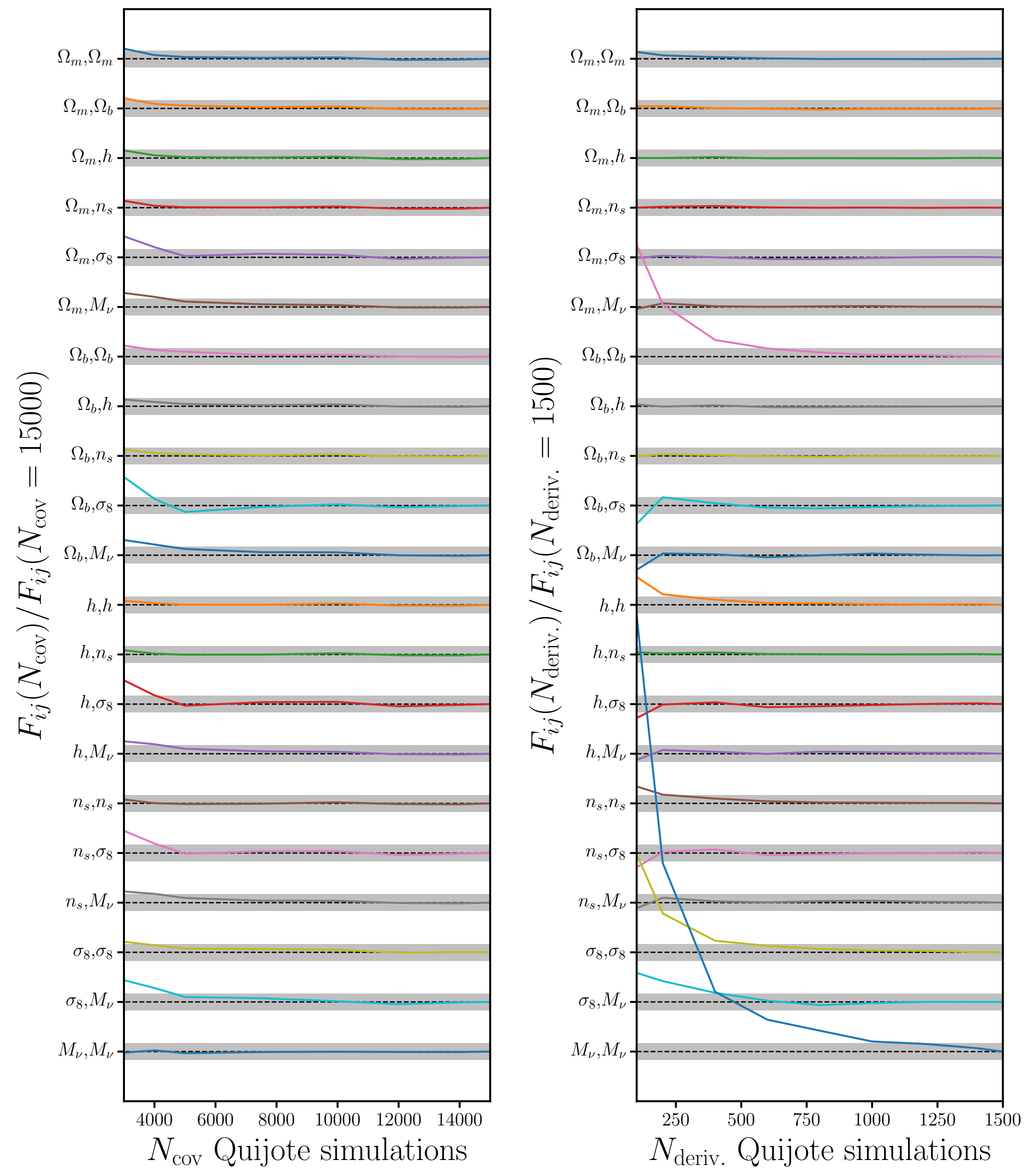

Brandbyge, J., Hannestad, S., Haugbølle, T., & Thomsen, B. 2008, Journal of Cosmology and Astro-Particle Physics, 08, 020

Carron, J. 2013, Astronomy & Astrophysics, 551, A88

Castorina, E., Sefusatti, E., Sheth, R. K., Villaescusa-Navarro, F., & Viel, M. 2014, Journal of Cosmology and Astro-Particle Physics, 02, 049

Chan, K. C., & Blot, L. 2017, Physical Review D, 96, arXiv:1610.06585

Davis, M., Efstathiou, G., Frenk, C. S., & White, S. D. M. 1985, The Astrophysical Journal, 292, 371

Dodelson, S. 2003, Modern Cosmology

Gil-Marín, H., Percival, W. J., Verde, L., et al. 2017, Monthly Notices of the Royal Astronomical Society, 465, 1757

Heavens, A. 2009, arXiv:0906.0664 [astro-ph], arXiv:0906.0664 [astro-ph]

Hockney, R. W., & Eastwood, J. W. 1981, Computer Simulation Using Particles

Ichiki, K., & Takada, M. 2012, Physical Review D, 85, 063521

Jungman, G., Kamionkowski, M., Kosowsky, A., & Spergel, D. N. 1996, Physical Review D, 54, 1332

Karagiannis, D., Lazanu, A., Liguori, M., et al. 2018, Monthly Notices of the Royal Astronomical Society, 478, 1341

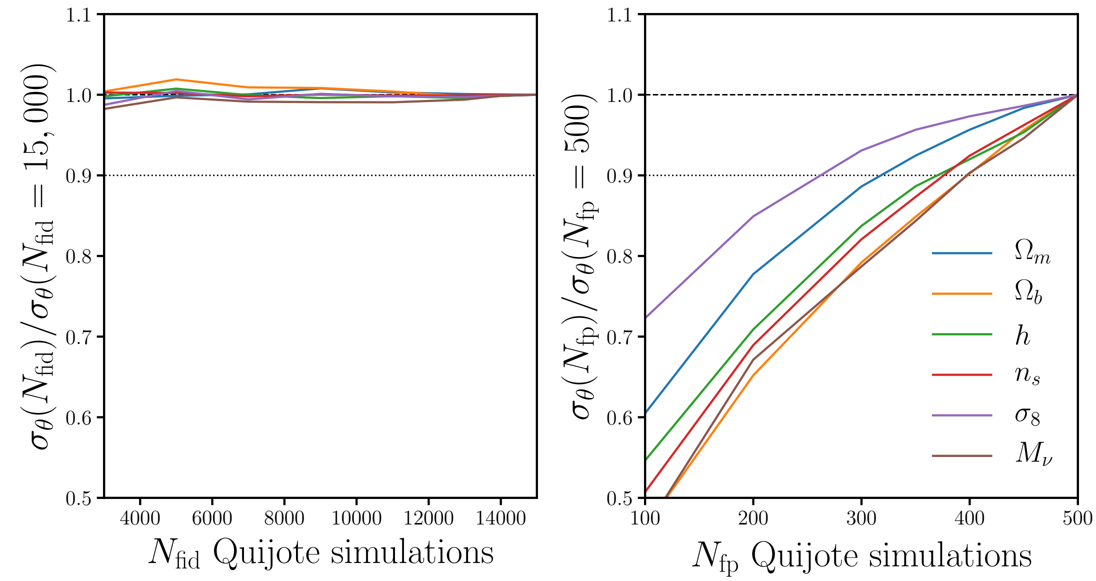

Figure 10. Left: The ratio of the 1σ Fisher constraint for $\theta = \Omega_{\rm m}, \Omega_{\rm b}, h, n_s, \sigma_8$, and M_ν calculated using $N_{\rm fid}$ Quijote simulations over the constraint calculated with all 15,000 simulations, $\sigma_\theta(N_{\rm fid})/\sigma_\theta(N_{\rm fid} = 15,000)$, as a function of $N_{\rm fid}$. The $N_{\rm fid}$ simulations are used to estimate $\boldsymbol{C}$ used to calculate the Fisher matrix (Eq. 10). The Fisher parameter constraints vary by < 10 and 1% for $N_{\rm fid} > 7000$ and $14,000$, respectively. **Right**: The ratio of the 1σ Fisher constraint for θ calculated using $N_{\rm fp}$ simulations over the constraint calculated with all 500 fixed paired simulations, $\sigma_\theta(N_{\rm fp})/\sigma_\theta(N_{\rm fp} = 500)$, as a function of $N_{\rm fp}$. The $N_{\rm fp}$ fixed paired simulations are used to numerically estimate $\partial B_0/\partial\theta_i$ in Eq. 10. Although $\sigma_\theta(N_{\rm fp})/\sigma_\theta(N_{\rm fp} = 500)$ vary among the parameters, for $N_{\rm fp} > 400$ and 450 they vary by < 10 and 5%, respectively. Hence, *we have a sufficient number of simulations to estimate* $\boldsymbol{C}$ *and the derivatives of the bipsectrum and our forecasts are robust to their convergence.*

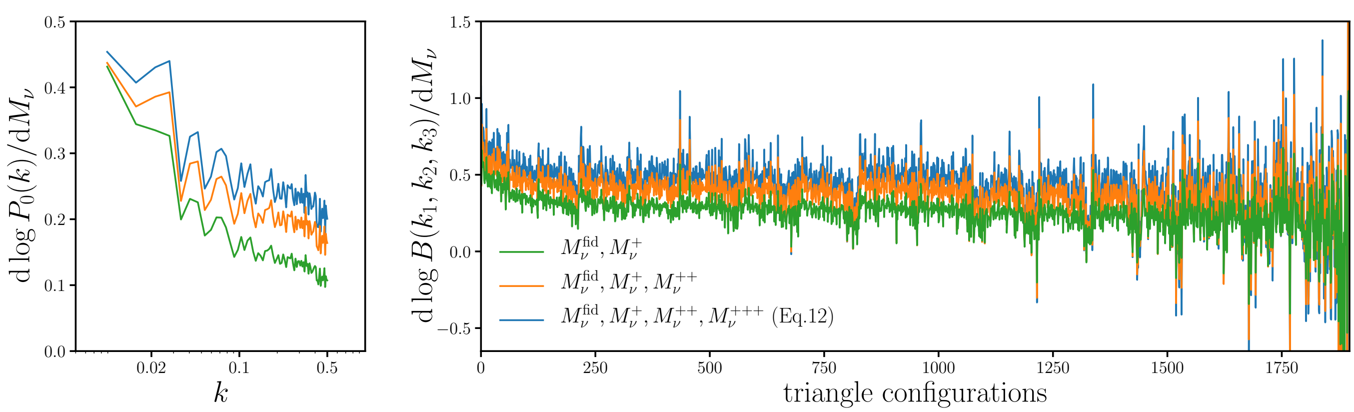

Figure 11. Comparison of $\partial \log B(k_1, k_2, k_3)/\partial M_\nu$ (right) and $\partial \log P(k)/\partial M_\nu$ (left), computed using Eq.12 (blue), excluding M_ν^{+++} (orange), and the forward difference approximation (green).

Leauthaud, A., Tinker, J., Bundy, K., et al. 2012, The Astrophysical Journal, 744, 159

LoVerde, M. 2014, Physical Review D, 90, 083518

Pontzen, A., Slosar, A., Roth, N., & Peiris, H. V. 2016, Physical Review D, 93, 103519

Ruggeri, R., Castorina, E., Carbone, C., & Sefusatti, E. 2018, Journal of Cosmology and Astroparticle Physics, 2018, 003

Scoccimarro, R. 2015, Physical Review D, 92, arXiv:1506.02729

Scoccimarro, R., Sefusatti, E., & Zaldarriaga, M. 2004, Physical Review D, 69, 103513

Sefusatti, E., Crocce, M., Pueblas, S., & Scoccimarro, R. 2006, Physical Review D, 74, arXiv:astro-ph/0604505

Sefusatti, E., Crocce, M., Scoccimarro, R., & Couchman, H. M. P. 2016, Monthly Notices of the Royal Astronomical Society, 460, 3624

Sefusatti, E., & Komatsu, E. 2007, Physical Review D, 76, 083004

Sefusatti, E., & Scoccimarro, R. 2005, Physical Review D, 71, arXiv:astro-ph/0412626

Song, Y.-S., Taruya, A., & Oka, A. 2015, Journal of Cosmology and Astro-Particle Physics, 2015, 007

Springel, V. 2005, Monthly Notices of the Royal Astronomical Society, 364, 1105

Tegmark, M., Taylor, A. N., & Heavens, A. F. 1997, The Astrophysical Journal, 480, 22

Tellarini, M., Ross, A. J., Tasinato, G., & Wands, D. 2016, Journal of Cosmology and Astro-Particle Physics, 2016, 014

Tinker, J. L., Leauthaud, A., Bundy, K., et al. 2013, The Astrophysical Journal, 778, 93

Vakili, M., & Hahn, C. 2019, The Astrophysical Journal, 872, 115

Verde, L. 2010, arXiv:0911.3105 [astro-ph], 800, 147

Viel, M., Haehnelt, M. G., & Springel, V. 2010, Journal of Cosmology and Astro-Particle Physics, 06, 015

Villaescusa-Navarro, F., Banerjee, A., Dalal, N., et al. 2018, The Astrophysical Journal, 861, 53

Villaescusa-Navarro, F., Marulli, F., Viel, M., et al. 2014, Journal of Cosmology and Astro-Particle Physics, 03, 011

Wolz, L., Kilbinger, M., Weller, J., & Giannantonio, T. 2012, Journal of Cosmology and Astroparticle Physics, 2012, 009

Yamauchi, D., Yokoyama, S., & Takahashi, K. 2017, Physical Review D, 95, 063530

Yankelevich, V., & Porciani, C. 2019, Monthly Notices of the Royal Astronomical Society, 483, 2078

Zennaro, M., Bel, J., Villaescusa-Navarro, F., et al. 2017, Monthly Notices of the Royal Astronomical Society, 466, 3244

Zentner, A. R., Hearin, A., van den Bosch, F. C., Lange, J. U., & Villarreal, A. 2016, arXiv:1606.07817 [astro-ph], arXiv:1606.07817 [astro-ph]

Zheng, Z., Berlind, A. A., Weinberg, D. H., et al. 2005, The Astrophysical Journal, 633, 791